

Direct numerical simulation of turbulent non-Newtonian flow using a spectral element method

M. Rudman *, H.M. Blackburn

CSIRO Manufacturing and Infrastructure Technology, P.O. Box 56, Highett Victoria 3190, Australia

Received 16 July 2004; accepted 10 November 2005

Available online 18 April 2006

Abstract

A spectral element—Fourier method (SEM) for Direct Numerical Simulation (DNS) of the turbulent flow of non-Newtonian fluids is described and the particular requirements for non-Newtonian rheology are discussed. The method is implemented in parallel using the MPI message passing kernel, and execution times scale somewhat less than linearly with the number of CPUs, however this is more than compensated by the improved simulation turn around times. The method is applied to the case of turbulent pipe flow, where simulation results for a shear-thinning (power law) fluid are compared to those of a yield stress (Herschel–Bulkley) fluid at the same generalised Reynolds number. It is seen that the yield stress significantly dampens turbulence intensities in the core of the flow where the quasi-laminar flow region there co-exists with a transitional wall zone. An additional simulation of the flow of blood in a channel is undertaken using a Carreau–Yasuda rheology model, and results compared to those of the one-equation Spalart–Allmaras RANS (Reynolds-Averaged Navier–Stokes) model. Agreement between the mean flow velocity profile predictions is seen to be good. Use of a DNS technique to study turbulence in non-Newtonian fluids shows great promise in understanding transition and turbulence in shear thinning, non-Newtonian flows.

© 2006 Elsevier Inc. All rights reserved.

1. Introduction

The flow of non-Newtonian fluids occurs in a wide range of practical applications including pipeline transport in the process industries, polymer processing and in many biological applications including the flow of blood through the body and in devices such as artificial hearts. If the fluid has a significant yield stress, or if its effective viscosity is high, flow rates may occur in a laminar flow regime. In such cases, if the rheology is known, computational simulation can be undertaken in a straightforward and reliable manner. However sometimes the flow can be transitional or turbulent and in such cases, the development of mathematical and computational models for turbulent non-Newtonian fluids is not sufficiently well advanced to allow RANS (Reynolds-Averaged Navier–Stokes) simulation to be undertaken.

* Corresponding author.

E-mail address: murray.rudman@csiro.au (M. Rudman).

Some experimental measurement of velocity profiles and turbulence statistics has appeared on the transitional and turbulent flow of non-Newtonian fluids [1–3] using optically clear polymer solutions. One of the difficulties in experimentation is designing suitable fluids that have well defined rheological properties that can be adjusted as required. It is not usually possible to do this, for example increasing the concentration of a polymer is likely to modify the shear-thinning index, consistency and yield stress simultaneously. Additionally, many polymer additives can produce fluids with some degree of visco-elasticity. Although the level of visco-elasticity may be irrelevant in low shear, laminar flow, it may become important in the high shear typical of turbulent flow.

Computational modelling of non-Newtonian fluids using direct numerical simulation (DNS) shows promise in helping to understand transition and turbulence in these flows. One key benefit of modelling is that once a rheological model is chosen, the effect of varying rheological parameters can be unambiguously determined. There have been some DNS of the turbulent flow of polymer solutions (e.g. [4–7]). With the exception of [6], these studies considered the drag reduction that arises in dilute polymer solutions in which shear-thinning behaviour was unimportant and visco-elastic effects were taken into account. For a wide range of important materials, the non-Newtonian rheology is primarily of a shear-thinning nature. Malin [8] considered turbulent pipe flow of power law fluids using a Reynolds-averaged approach and a modified $k-\epsilon$ model. Reasonable agreement with experimental data was obtained after modifying the wall damping functions. Apart from [6] there have been few published CFD investigations of the turbulent flow of shear-thinning non-Newtonian fluids without visco-elasticity.

The purpose of this paper is threefold. First, the numerical method used in [6] is described in detail with particular reference to the requirements for simulating non-Newtonian fluids. The parallel performance of the method is also quantified. Second, the flow of shear-thinning fluids with and without the presence of a yield stress is considered, with particular emphasis on the qualitative and quantitative effects that yield stress has on mean flow profiles and turbulence structure. Third, the data from these simulations will be useful as calibration/comparison data when considering the application of Reynolds-Averaged Navier–Stokes (RANS) simulations. An additional example of turbulent non-Newtonian fluid, simulation of the flow of blood in a channel geometry is also presented, specifically because one-equation RANS modelling is available for this case (see [9]).

2. Problem description

The shear-thinning non-Newtonian fluids considered in this study are ones whose rheology is described by a generalised Newtonian model. Such fluids have an isotropic viscosity that is a function of flow properties. The fluid stress tensor is written as the product of this viscosity and the rate-of-strain tensor,

$$\tau_{ij} = \eta S_{ij}. \quad (1)$$

Three different rheology models are considered, the power law, Herschel–Bulkley and Carreau–Yasuda models all of which are dependant on a shear rate, $\dot{\gamma}$, that is defined as the second invariant of the rate-of-strain tensor

$$\dot{\gamma} = \left(2 \sum_{i,j} S_{ij} S_{ji} \right)^{\frac{1}{2}}. \quad (2)$$

The Herschel–Bulkley model is written

$$\eta = \frac{\tau_Y}{\dot{\gamma}} + K \dot{\gamma}^{n-1}, \quad (3)$$

where K is the consistency, n is the flow index, and τ_Y is the fluid yield stress. A power law model is obtained from the Herschel–Bulkley model by setting the yield stress to zero.

The Carreau–Yasuda model is written

$$\eta = \eta_{\infty} + \frac{\eta_0 - \eta_{\infty}}{(1 + (\lambda \dot{\gamma})^b)^a}, \quad (4)$$

where η_0 and η_{∞} are the zero shear and infinite-shear plateau viscosities, and λ , a and b are fitting parameters.

2.1. Generalised Reynolds number

Definition of a Reynolds number in a flow in which the viscosity of the fluid varies in space and time is not unique as many viscosity scales can be chosen. A discussion of the different options for wall bounded flows is given in [6]. A useful choice is to use the mean wall viscosity, η_w . For pipe and channel flow, the relationship between the mean viscous stress at the wall and the applied pressure gradient is easily determined ($\tau_w = D/4\partial P/\partial z$ for pipe flow and $D\partial P/\partial z$ for channel flow where D is pipe diameter or channel half width). Once the pressure gradient is known, an estimate of the mean wall shear stress and hence mean wall viscosity can be made. For a Herschel–Bulkley fluid, this can be determined a priori using

$$\eta_w = \frac{K^{1/n}\tau_w}{(\tau_w - \tau_Y)^{1/n}}. \quad (5)$$

For the Carreau–Yasuda model, a fixed-point iterative numerical approach is used in which Eq. (4) is solved at the wall using the known value of the wall shear stress and recalling that for all generalised Newtonian fluids $\tau_w = \eta_w \dot{\gamma}_w$.

For Newtonian fluids, the Blasius relationship can be used to determine the mean (or superficial) flow velocity in a pipe or channel. For a generalised Newtonian fluid, it is not possible in general to determine the mean velocity a priori. Correlations proposed in [10] for power law fluids and in [11] for Herschel–Bulkley fluids, provide estimates that are within 5–10% of the predicted values for all simulations here. For the Carreau–Yasuda model, a reasonable estimate (also within 10%) was achieved by using the infinite-shear viscosity, η_∞ in the Blasius correlation. The accuracy of this approach in general is not known, and will depend on the range of shear rates expected in the flow and the width and steepness (in terms of $\dot{\gamma}$) of the transition from zero-shear to infinite-shear viscosity.

Once the wall viscosity and mean velocity are known (or determined from the simulation), the generalised Reynolds number is written

$$Re_G = \frac{\rho U D}{\eta_w}. \quad (6)$$

This generalised Reynolds number reflects flow behaviour in the near-wall region that plays a fundamental role in transition and the development of turbulence in wall bounded flows of Newtonian fluids, and is used here as a basis on which to compare results for different rheology fluids. It was shown in [6] to collapse the data quite well for the flow of power-law fluids.

For pipe flow of power law fluids it is common to present results in terms of the Metzner–Reed Reynolds number, Re_{MR} . A similar Reynolds number can be defined for Herschel–Bulkley fluids using the method proposed in [12]. Although this is not strictly the same as the Metzner–Reed Reynolds number, it will be termed Re_{MR} , to avoid introducing additional terminology that could obscure the emphasis of the discussion.

2.2. Wall units

Wall units are introduced in a similar manner to the Newtonian analysis with the wall viscosity taking the place of the Newtonian viscosity. Hence the friction velocity is defined as $U_\tau = \sqrt{\tau_w/\rho}$, the non-dimensional velocity is $U^+ = U/U_\tau$ and the non-dimensional distance from the wall is written $y^+ = (\rho U_\tau / \eta_w)y$ (or $y^+ = (\rho U_\tau / \eta_w)(R - r)$ for pipe flow, where R , is the pipe radius).

3. Numerical method

3.1. Spectral element—Fourier discretisation

The three-dimensional spatial discretisation uses isoparametrically mapped quadrilateral spectral elements to subdivide the domain in two dimensions, (x, y) , coupled with Fourier expansions in an orthogonal direction, z , in which the flow can be assumed periodic [13]. Standard nodal spectral elements are used, for which in the master element space $[-1, 1] \times [-1, 1]$ the shape functions are formed as tensor products of Lagrange

interpolants on the Gauss–Lobatto–Legendre (GLL) quadrature points. The quadrature used for the weak form of the Galerkin treatment of elliptic equations is carried out via GLL weights. A convenient consequence of using GLL Lagrange interpolants and GLL quadrature is that the mass matrices in such a formulation are diagonal.

3.2. Velocity-correction time integration

Time integration is carried out using a second-order time integration scheme [14] based on operator splitting. This has been recently characterised as one of a class of velocity (as opposed to pressure) correction projection schemes [15]. The time-step begins by computing an intermediate velocity field approximated to the end of the current time-step, n ,

$$\mathbf{u}^* = - \sum_{q=1}^J \alpha_q \mathbf{u}^{(n-q)} - \Delta t \sum_{q=0}^{J-1} \beta_q [N(\mathbf{u}^{(n-q)}) - 2\nabla \cdot (\mathbf{v}^{(n-q)} - v_{\text{ref}}) \mathbf{S}^{(n-q)}],$$

where $N(\mathbf{u}^{(n-q)})$ represents the nonlinear advection terms from time level $(n - q)$, which are computed in skew-symmetric form $(\mathbf{u} \cdot \nabla \mathbf{u} + \nabla \cdot \mathbf{u}\mathbf{u})/2$ in order to reduce aliasing errors and promote stability. The viscous stress terms are dealt with by splitting them into a component computed with constant reference viscosity, v_{ref} , and a component computed with spatially variable viscosity v , derived from the velocity field through a rheology model, an approach originally to applied to treatment of sub-grid scale stresses in large eddy simulation [16]. The rate-of-strain tensor $S = [\nabla \mathbf{u} + (\nabla \mathbf{u})^T]/2$ is the symmetric part of the velocity gradient tensor. Here, the time-order of the scheme, J , is set to two for the current computations, and the values of the discrete weights α_q and β_q appear for example in [14]. The intermediate velocity field is used as forcing for the solution of a pressure Poisson equation

$$\nabla^2 p^{(n+1)} = \frac{\rho}{\Delta t} \nabla \cdot \mathbf{u}^*,$$

with the high-order Neumann pressure boundary condition

$$\partial_n p^{(n+1)} = -\rho \mathbf{n} \cdot \sum_{q=0}^{J-1} \beta_q [N(\mathbf{u}^{(n-q)}) + v \nabla \times \nabla \times \mathbf{u}^{(n-q)} + \partial_t \mathbf{u}^{(n-q)}],$$

applied on walls. Following computation of the pressure, its gradient is used to update the intermediate velocity field through

$$\mathbf{u}^{**} = \mathbf{u}^* - \frac{\Delta t}{\rho} \nabla p^{(n+1)}$$

and finally a viscous correction is applied through the solution of a set of scalar Helmholtz equations for each velocity component

$$\nabla^2 \mathbf{u}^{(n+1)} - \frac{\alpha_0}{v \Delta t} \mathbf{u}^{(n+1)} = - \frac{\mathbf{u}^{**}}{v_{\text{ref}} \Delta t},$$

where v_{ref} is the spatially constant reference kinematic viscosity, typically set to be larger than the maximum kinematic viscosity computed through the rheology model.

In the above, there are two elliptic equations to be solved, one for the pressure, and the other for the viscous correction. These are solved for each two-dimensional complex Fourier mode using a Galerkin method and integration by parts over the two-dimensional (x, y) domain Ω , which are standard finite-element techniques. The structure of one of these equations, for Fourier mode k , is

$$\int_{\Omega} \partial_x \phi \partial_x \hat{c}_k + \partial_y \phi \partial_y \hat{c}_k + (\beta^2 k^2 + \lambda) \phi \hat{c}_k \, d\Omega = - \int_{\Omega} \phi \hat{f}_k \, d\Omega + \int_{\Gamma_N} \phi h \, d\Gamma,$$

where \hat{c}_k is a two-dimensional complex scalar field (representing the solution variable) and ϕ is a weight function: under Galerkin treatment, these both satisfy identical Dirichlet (‘essential’) boundary conditions. The Fourier constant $\beta = 2\pi/L$, where L is the length of the domain in the z direction, while the Helmholtz

constant $\lambda = \alpha_0/v_{ref}\Delta t$ for the viscous Helmholtz equation, but is zero for the pressure Poisson equation. On the right-hand-side, \hat{f}_k is a complex scalar forcing field, while h represents Neumann boundary conditions on boundary segment Γ_N .

3.3. Computation and treatment of spatially variable viscosity

Because both the power law and Herschel–Bulkley rheology models have a singular viscosity at zero shear rate, a ‘cut-off’ value is used, below which the shear rate is assumed to be constant when computing the viscosity. The cut-off value is chosen to be 10^{-5} times the mean shear rate and is not observed to cause any stability problems or significant errors. The cut-off is almost never invoked in practice for either the Herschel–Bulkley or Carreau–Yasuda simulations because the calculated shear rates throughout the flow (even in the less active core regions) are nearly always several orders of magnitude above the cut-off value.

3.4. Memory exchanges for parallel solution

For most of the computations within each time-step, data are held in the Fourier-transformed state, i.e. as a set of two-dimensional complex modes (pairs of data planes), with each process/CPU holding a subset. However, nonlinear product terms, and the magnitude of the strain rate, $|S| = (S_{ij}S_{ij})^{1/2}$, are computed pseudo-spectrally, in physical space. In order to be able to compute the Fourier transforms to and from physical space, each process must have available all modes/planes at some subset of physical space locations, thus data must be exchanged across processes. The layout of memory across processes before and after exchange is illustrated schematically in Fig. 1, for six planes (three modes) of data, z_0 – z_5 , distributed across three processes, PROC_0–PROC_2. The data in each plane are divided into the same number of (approximately equal-sized) blocks of data, b_0 – b_2 ; there is the same number of blocks as processes, and block boundaries do not have to coincide with element boundaries.

The method of exchange (for the data layout of Fig. 1) is illustrated in Table 1. Initially (a), each process has two z -planes of data; within each plane, data are ordered by block index, so that block index varies most rapidly as memory is traversed. In the first step (b), data are locally reordered on each process so that the blocks are grouped together, with plane index varying most rapidly. Finally (c), memory is exchanged across processes in a block transpose, so that each process ends up with all the data for a single block. The transposition is carried out efficiently by message passing: the comparatively small number of large-sized blocks means that communication bandwidth is much more important than latency.

In order to compute the nonlinear terms in skew-symmetric form, 18 memory exchanges (for an amount of data equivalent to that for a single scalar component) are required per time-step.

3.5. Parallel performance

All computations reported here were performed on the Australian Partnership for Advanced Computing (APAC) SC cluster, most using 32 CPUs. This machine consists of 127 nodes, each with four 1 GHz ev68

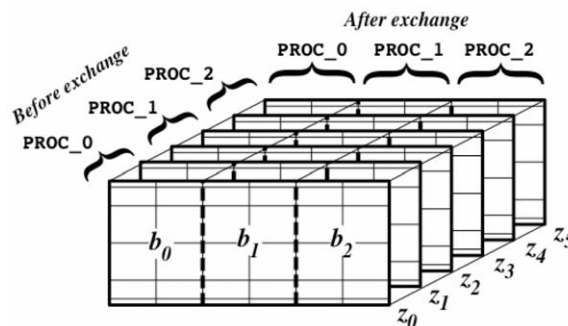


Fig. 1. Arrangements of six data planes of memory, distributed across three processes, before and after exchange.

Table 1

Illustration of how initial layout of data (a) is first re-ordered locally on each process (b), followed by transposition across processes (c)

PROC_0			PROC_1			PROC_2			PROC_0			PROC_1			PROC_2											
p_0	b_0	z_0	p_1	b_0	z_2	p_2	b_0	z_4	p_0	b_0	z_0	p_1	b_0	z_2	p_2	b_0	z_4	p_0	b_0	z_0	p_0	b_1	z_0	p_0	b_2	z_0
p_0	b_1	z_0	p_1	b_1	z_2	p_2	b_1	z_4	p_0	b_0	z_1	p_1	b_0	z_3	p_2	b_0	z_5	p_0	b_0	z_1	p_0	b_1	z_1	p_0	b_2	z_1
p_0	b_2	z_0	p_1	b_2	z_2	p_2	b_2	z_4	p_0	b_1	z_0	p_1	b_1	z_2	p_2	b_1	z_4	p_1	b_0	z_2	p_1	b_1	z_2	p_1	b_2	z_2
p_0	b_0	z_1	p_1	b_0	z_3	p_2	b_0	z_5	p_0	b_1	z_1	p_1	b_1	z_3	p_2	b_1	z_5	p_1	b_0	z_3	p_1	b_1	z_3	p_1	b_2	z_3
p_0	b_1	z_1	p_1	b_1	z_3	p_2	b_1	z_5	p_0	b_2	z_0	p_1	b_2	z_2	p_2	b_2	z_4	p_2	b_0	z_4	p_2	b_1	z_4	p_2	b_2	z_4
p_0	b_2	z_1	p_1	b_2	z_3	p_2	b_2	z_5	p_0	b_2	z_1	p_1	b_2	z_3	p_2	b_2	z_5	p_2	b_0	z_5	p_2	b_1	z_5	p_2	b_2	z_5

(Alpha 21264C) cpus with a Quadrics Elan3 interconnect. Run times were typically in the order of 2000 CPU hours to reach a statistically steady state, with an additional 2000–2500 CPU hours used to obtain turbulence statistics. These latter times corresponded to 8–10 fluid transit times over the length of the computational domain.

The parallel performance of the implementation is shown in Table 2 where the CPU time per time-step per million grid nodes is compared as a function of number of CPUs. The simulation contained 4.8 million grid nodes and was run for a minimum of 500 time-steps to obtain efficiency statistics. Because the number of Fourier modes was 192, the maximum number of processors available on the SC system for this simulation was 48. The parallel efficiency is defined to be the total CPU time for N processors divided by the total CPU time for one processor expressed as a percentage. As can be seen, the scaling with number of CPUs is less than linear, with a 48 CPU job running with approximately 56% of the efficiency of the single CPU run. However, the 48 CPU computation completes in an elapsed time approximately 30 times less than a single run, resulting in significantly more rapid turn-around.

3.6. Validation, grid refinement and domain size

The underlying numerical code has been validated for both DNS and LES of pipe and channel flow of turbulent Newtonian fluids [17–19]. Implementation of the non-Newtonian viscosity implementation was validated for power-law fluids against laminar pipe flow and axisymmetric Taylor–Couette flow both of which have analytic solutions. For the Herschel–Bulkley model, validation was against laminar pipe flow, and apart from ensuring correct viscosity estimates for known shear fields, nothing additional was done for the Carreau–Yasuda model. In all laminar simulation cases, numerical and theoretical velocity profiles agreed to within 0.01% and the code is believed to be accurately predicting the laminar flow of non-Newtonian fluids with generalised Newtonian rheologies.

Validation for the turbulent flow of non-Newtonian fluids is difficult due to the scarcity of published velocity profiles and turbulence statistics. Results reported in [6] suggest that the technique is correctly predicting turbulent flow of power law fluids, although discrepancies arose in that study as a result of elastic effects in the experiments that are not accounted for in the DNS method.

Table 2
CPU timing and parallel efficiency

No. CPUs	Total CPU time per time-step per million grid nodes (s)	Parallel efficiency (%)	Total CPU time per 1000 time-steps (hours)	Wall time per 1000 time-steps (hours)
1	17.6	100	24.3	24.3
2	19.5	90	26.4	13.3
4	19.8	88	26.8	6.7
8	23.1	76	31.3	4.1
16	28.6	62	38.7	2.5
32	30.6	58	41.5	1.3
48	31.7	56	43.0	0.9

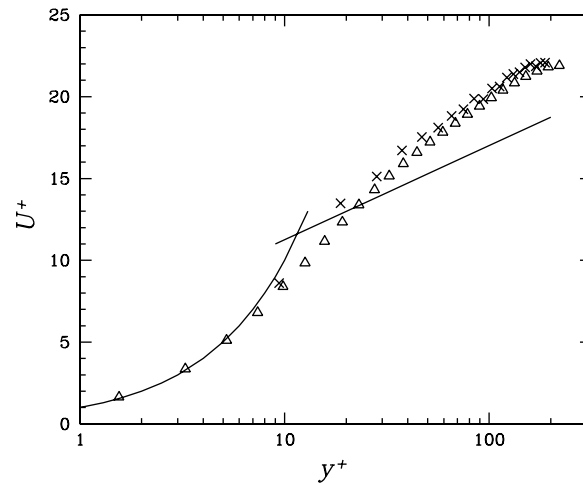


Fig. 2. Comparison of mean velocity profile in wall units for experiment measurements of an Ultrez 10 solution (×) and DNS (Δ). The solid line is the Newtonian law-of-the wall profile.

Comparisons were also presented in [6] comparing the DNS with experimental results for the flow of a 0.05 wt% Ultrez 10 solution, a fluid that is well-approximated with a Herschel–Bulkley rheology model. The rheology parameters used for the DNS in [6] were based on viscometry measurements of a fluid sub-sample taken at the start of the pipe tests. The comparison in [6] was seen to be reasonable, but re-analysis of the experimental data has shown that this rheology does not agree with the laminar pipe flow data measured in the experiments. The pipe data is a more reliable indicator of the actual rheology of the fluid in the pipe tests, especially as the Ultrez has a tendency to break down after repeated pumping. A fit to the pipe data provides Herschel–Bulkley coefficients of $\tau_Y = 1.28$ Pa, $k = 1.10$ and $n = 0.52$ and these were used in a new validation simulation to compare to the experimental results for turbulent flow. The comparison is shown in Fig. 2 where the agreement for the mean velocity profile is seen to be good. Consequently, confidence in the results of the DNS method for Herschel–Bulkley fluids is warranted.

A grid convergence study was also reported in [6], and the resolution used below (in terms of wall units) is slightly better than the resolution required to obtain grid independence of the second order turbulence statistics demonstrated in [6]. Because a periodic domain is being used for these simulations, the possibility of domain length effects influencing the results is also possible, and this is addressed in more detail in examples discussed below.

4. Turbulent pipe flow

For the pipe flow simulations, the computational domain consists of 105 10th-order elements in the pipe cross-section (see [6]) and 192 Fourier modes (i.e. 384 data planes) in the axial direction, with a domain length of $5\pi D$. A nominal bulk flow generalised Reynolds number of 7500 was chosen and the resulting parameter estimation (based on correlations in [10] and [11]) for the simulations considered here are shown in Table 3.

Table 3

Non-dimensional parameters for the pipe flow simulations (note that $n = 0.6$, the nominal Re_G is 7500 and the non-dimensionalised pipe diameter and expected superficial flow velocity are both 1)

Sim.	τ_Y	K	$\partial P/\partial z$	τ_w	Actual W	Re_G	Re_{MR}
Newton	0.0	1.333×10^{-3}	1.670×10^{-2}	4.175×10^{-3}	0.983	7370	7370
PL	0.0	5.002×10^{-4}	1.454×10^{-2}	3.634×10^{-3}	0.989	7414	4119
HB1	2.861×10^{-4}	4.230×10^{-4}	1.223×10^{-2}	3.057×10^{-3}	0.945	7088	4032
HB2	8.540×10^{-4}	2.948×10^{-4}	1.044×10^{-2}	2.610×10^{-3}	0.919	6894	3745

The actual predicted mean velocity (W) defines the predicted generalised Reynolds number.

The aim of these pipe flow simulations is to understand and quantify the effect that yield stress has on the turbulent pipe flow of shear-thinning fluids. Further, they provide calibration and/or validation data for comparison to RANS models of turbulent Herschel–Bulkley fluids. The power-law simulation (PL) at $n = 0.6$ is used as the base case, and at a generalised Reynolds number of 7500 the results shown below suggest this flow lies within the regime of well-developed turbulence. The two Herschel–Bulkley simulations utilise the same fluid rheology parameters as PL except with the inclusion of a yield stress. In the case of HB1, the fluid yield stress is set to be equal to 10% of the mean wall shear stress in PL, and in the case of HB2, the fluid yield stress is set to be 50% of the mean wall shear stress in PL. Note that in order to maintain the same generalised Reynolds number (7500) in the Herschel–Bulkley cases, the axial pressure gradient must be increased. As a consequence the non-dimensionalisation of the problem is changed, and the non-dimensional rheology parameters are also modified as the yield stress changes (as shown in Table 3). Results for a Newtonian fluid are also included for reference.

In terms of wall units defined earlier, the near-wall mesh spacing for the pipe flow simulations is given by $r^+ \approx 0.25$, $R\theta^+ \approx 7$, $z^+ \approx 11$, with coarser resolution in pipe cross-sections being applicable near the pipe centreline.

4.1. Mean flow profiles

The mean axial velocity for the three non-Newtonian simulations at Re_G nominally equal to 7500 are shown in Fig. 3 and compared to a Newtonian profile at the same Reynolds number. The results for HB2 fall sufficiently above the Newtonian profile to suggest that this flow is transitional – this point will be discussed in more detail below. Both the power law and lower yield stress results show indications of a log-layer profile with a greater slope than the Newtonian case. All simulations display linear behaviour in the near-wall sub-layer.

Fig. 4 shows the mean (non-dimensionalised) shear rate profile as a function of distance from the wall where the shear rate is seen to be close to constant only for a very small distance ($y^+ \approx 5$). The shear profiles are almost identical for all simulations up to approximately ($y^+ \approx 25$), where they begin to diverge from the Newtonian curve. At around $y^+ \approx 60$, the effect of yield stress begins to become apparent, with the predicted mean shear rate dropping far more rapidly with distance from the wall for the yield stress fluids.

Turbulence intensities, turbulence production, Reynolds shear stresses and total turbulent kinetic energy are plotted in Figs. 5 and 6. For both the axial turbulence intensities and the Reynolds stresses, the results

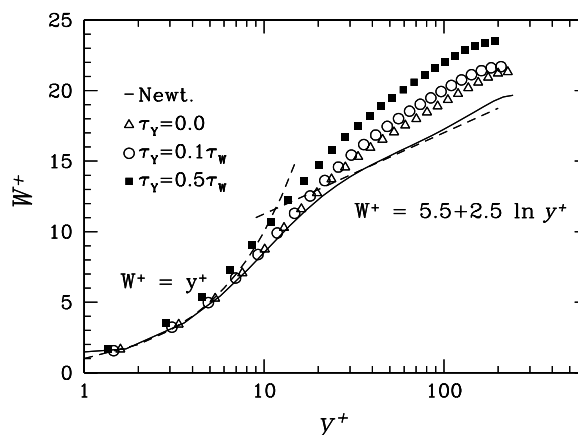


Fig. 3. Velocity profiles for the turbulent pipe flow of non-Newtonian fluids at $Re_G = 7500$. Solid line is the Newtonian profile, and symbols are (Δ) PL ($n = 0.6$, $\tau_Y = 0$), (\circ) HB1 ($n = 0.6$, $\tau_Y = 0.1\tau_w$) and (\blacksquare) HB2 ($n = 0.6$, $\tau_Y = 0.5\tau_w$). Profiles have been non-dimensionalised using conventional wall variables with the wall viscosity taking the place of the Newtonian viscosity. Shown for comparison (dashed line) is the linear wall profile and experimental log-law correlation for low Reynolds number turbulent pipe flow of a Newtonian fluid.

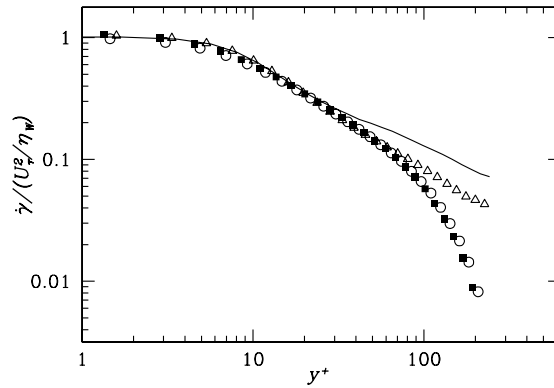


Fig. 4. Shear rate profiles ($\dot{\gamma}$) for the turbulent pipe flow of non-Newtonian fluids at $Re_G = 7500$. Solid line is the Newtonian profile, and symbols are (Δ) PL ($n = 0.6, \tau_Y = 0$), (\circ) HB1 ($n = 0.6, \tau_Y = 0.1\tau_w$) and (\blacksquare) HB2 ($n = 0.6, \tau_Y = 0.5\tau_w$). Profiles have been non-dimensionalised using mean wall shear rate determined from wall viscosity and shear stress.

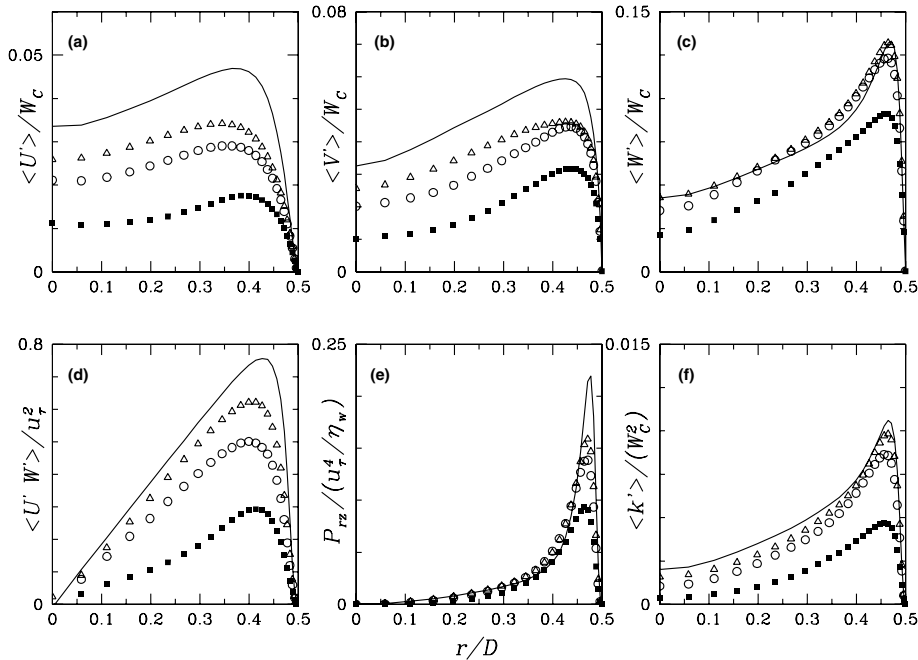


Fig. 5. Turbulence intensities as a function of r/D (a) radial, (b) azimuthal and (c) axial, (d) turbulence production, (e) Reynolds shear stress, and (f) total turbulent kinetic energy. (Solid line is Newtonian DNS, non-Newtonian fluids are (Δ) PL ($n = 0.6, \tau_Y = 0$), (\circ) HB1 ($n = 0.6, \tau_Y = 0.1\tau_w$) and (\blacksquare) HB2 ($n = 0.6, \tau_Y = 0.5\tau_w$)).

for the power law fluid are close to the Newtonian results (DNS at $Re = 7500$). However for both radial and azimuthal velocity fluctuations, the values for all of the non-Newtonian fluids are significantly lower than the Newtonian case, suggesting that the wall streaks are weaker for the non-Newtonian fluids. This behaviour has also been observed experimentally [2,3] in turbulent flow of non-Newtonian fluids, although currently there is no clear understanding of why this is the case. The presence of a yield stress has the effect of reducing the cross-stream turbulence intensities compared to the straight power-law case, with higher yield stresses reducing the cross-stream intensities more. Of interest is that the axial intensities (at least in the case of HB1) remain almost identical to the power law and Newtonian intensities except near the core of the flow where the shear rates are

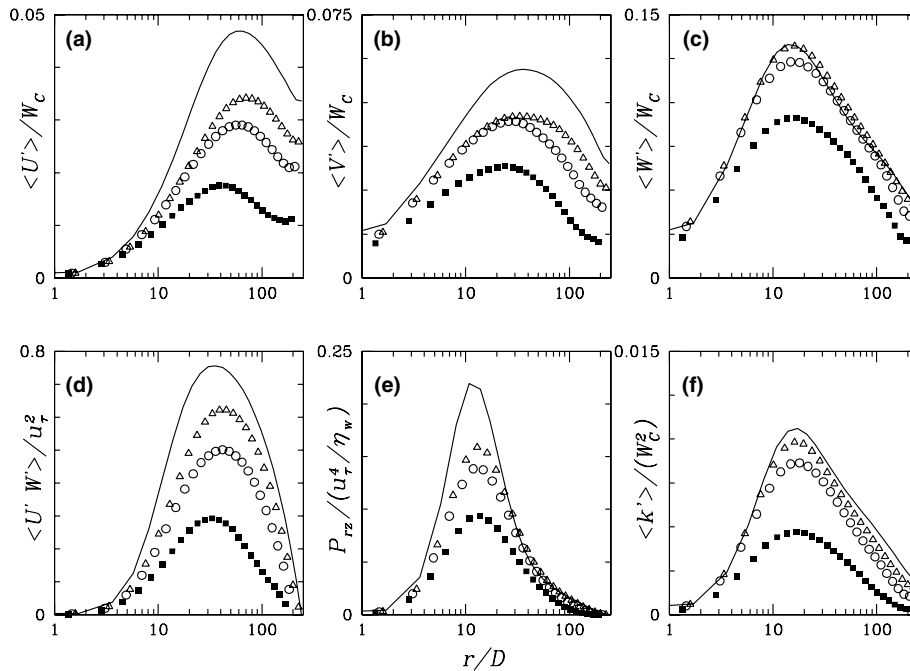


Fig. 6. As in Fig. 5 except plotted as a function of distance from the wall in wall units.

lower and the viscosity, consequently, higher. For HB2, turbulence intensities are lower than Newtonian for all components, again suggesting that this flow is transitional.

It has been observed [20] that low Reynolds number turbulence of Newtonian fluids has smaller (non-dimensionalised) cross-stream turbulence intensities compared to high Re Newtonian flows, but equivalent axial turbulence intensities. Thus the results seen in Figs. 5 and 6 are possibly features of flows that are not fully developed and in which a self-similar velocity profile is not yet established in the pipe. However, whether this is the cause of the trends predicted for the turbulence intensities for the Herchel-Bulkley fluids is not easily determined except by increasing Re_G significantly beyond what is currently possible with available computational resources.

The distance from the wall of the peak velocity fluctuations and Reynolds stress appears to decrease slightly (in wall units) as the yield stress increases. The location of maximum turbulence production

$$P_{rz} = \overline{U'_r W'_z} \frac{\partial \overline{W}}{\partial r} \quad (7)$$

occurs at a distance from the wall of $y^+ \approx 10$ for all results, (including Newtonian) suggesting that the non-dimensionalisation (based on mean wall viscosity) used for the non-Newtonian results is an appropriate one. One of the most obvious differences between these flows is seen in the turbulent kinetic energy, especially at the pipe centreline. It is slightly less for a power fluid than a Newtonian, is approximately halved for the addition of a small yield stress (HB1) and is approximately 1/8th the value for a yield stress equal to half the mean power law wall shear stress (HB2). This effect is intuitively what might be expected, because although the wall viscosity is the same for all cases, as the yield stress is increased, the effective viscosity in the core of the flow increases more rapidly. This is clearly illustrated in Fig. 7 where the mean viscosity as a function of radius is plotted for the three non-Newtonian simulations. Of note is the range of viscosities, with a factor of 4 difference in mean viscosity between the wall and centreline for the power law fluid (PL), whereas a factor of approximately 8 applies for a yield stress of $0.1\tau_w$ (HB1) and a factor of approximately 65 for a yield stress of $0.5\tau_w$ (HB2). Note the log scale on the vertical axis in Fig. 7. The mean viscosity averaged over the entire domain for the three non-Newtonian cases is approximately 2.5, 3.9 and 14.7 times the wall viscosity for PL, HB1 and HB2 respectively.

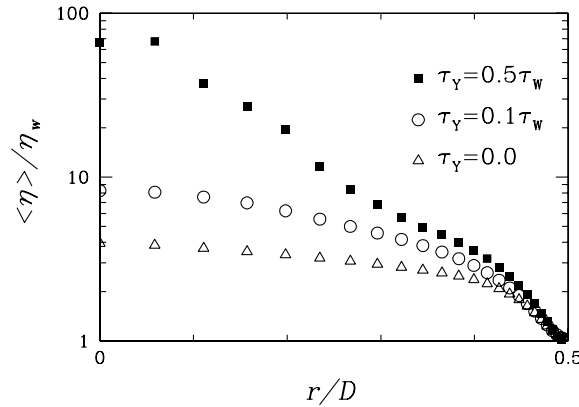


Fig. 7. Mean normalised viscosity as a function of radius for the non-Newtonian fluids at $Re_G = 7500$.

4.2. Friction factors

The Fanning friction factor, f , is the non-dimensional wall shear stress and is defined as

$$f = \tau_w / \rho \bar{W}^2. \tag{8}$$

For shear-thinning fluids, the friction factor is traditionally plotted against the Metzner–Reed Reynolds number. The results obtained numerically here are compared to the friction factors determined by Dodge and Metzner [21] for power law fluids in Fig. 8.

The numerical results predict friction factors that are lower than the corresponding values for a Newtonian fluid, with values decreasing with increasing yield stress. Qualitatively they agree with experimental observations [21] in which shear-thinning behaviour was seen to lead to a reduction in friction factor for a fixed Re_{MR} . Quantitatively, the predicted value for PL is about 10% higher than those measured in [21], although the values for the yield stress fluids are approximately 5% and 15% lower respectively. The reason for the lower friction factors for the yield stress fluids is related to the reduced turbulence intensities for these cases, with weaker turbulent structure bringing less high speed fluid from the core regions into the near-wall regions where wall

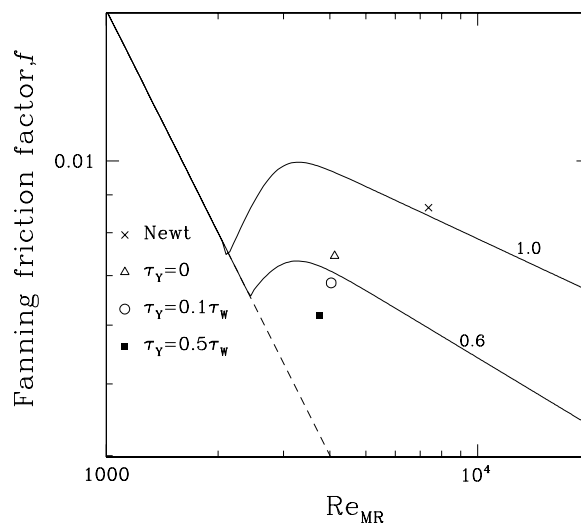


Fig. 8. Fanning friction factors determined for the CFD simulations as a function of the Metzner–Reed Reynolds number. The solid curves are for Newtonian fluid ($n = 1$) and a power-law fluids ($n = 0.6$). The friction factor decreases with yield stress, indicating a lower level of (non-dimensionalised) drag for higher yield stress materials.

drag is produced. Although this behaviour is qualitatively similar to the drag reduction caused by polymer additives (see [4,5]) it is not quantitatively the same. Drag reduction typically arises in low concentration solutions of an additive that has little or no effect on the shear viscosity of the carrier fluid (hence for the same pressure gradient, drag is reduced and flow is increased). In contrast, in the case here, an additive would need to modify the Newtonian rheology parameters shown in Table 3 to give the HB1 or HB2 parameters in order to qualify as a true drag reducing agent (i.e. it would need to provide a yield stress at the same time as reducing the consistency). Such behaviour seems rather unlikely in practice, and the apparent drag reduction seen in Fig. 8 is consequently an artefact of the non-dimensionalisation used to compare the results.

4.3. Intermittency and transition

Time traces of velocity signals for the simulations are shown in Fig. 9. Traces at the centreline (dashed line), log layer (dotted line) and near wall (solid line) are shown. There is a clear distinction between the results for the Newtonian and power law fluids, between the power law and yield stress fluids and between the two different yield stress fluids. The Newtonian fluid is clearly fully developed turbulence at this Reynolds number and displays a random, short-time fluctuation in both velocity components at all locations. The power law results are similarly random and unsteady, although the time scale of the fluctuations is significantly longer, suggesting that the unsteady structures have a larger size than in the case of the Newtonian fluid. For HB1, the level of unsteadiness drops further, and there are clear signs of large scale structure in the signals that corresponds approximately to the domain transit time (especially for the near-wall velocity traces), suggesting that domain length effects are probably influencing the results here. There is still significant random unsteadiness away from the walls, suggesting the flow is fairly turbulent, although not fully developed. For the higher yield stress fluid (HB2), the flow is clearly transitional, with obvious patches of unsteadiness followed by periods of relative quiescence. Domain length effects are clearly visible here in all velocity traces, with the period between disturbances approximately equal to the domain transit time.

Contours of axial velocity at $y^+ \approx 20$ are shown in Fig. 10. The turbulent structures seen in these images are consistent with the time traces in Fig. 9. The structure in the Newtonian case is clearly small scale and turbulent, similarly in the case of the power law fluid although the structures are both longer and wider (and according to the turbulence intensities shown in Figs. 5 and 6, also weaker). In the case of HB1, the distribution of turbulent structure is becoming less uniform and for HB2, there is clearly one single, large spiral structure that spans the entire computational domain (note that the pipe surface has been rolled flat in these images). This large structure is self-sustaining for many domain transit times and provides features of intermittency for a stationary observer. This last flow is clearly transitional and the domain length is insufficient to provide a reliable simulation of this flow. However, results presented in [6] for a transitional power law fluid suggest that despite the domain length limitations, the mean flow statistics (both first and second order) are still accurately represented by the simulation results, and that transition is likely to occur via intermittent phenomena such as turbulent puffs observed in Newtonian turbulence. However it is occurring here at a generalised Reynolds number that is significantly higher than that observed for Newtonian flow. Longer domain length simulations were not feasible here because of the Reynolds number being considered and the accompanying computational limitations.

Instantaneous snapshots of cross-sectional velocities, contours of axial velocity and contours of viscosity are shown in Fig. 11. The contour scales are identical for each fluid and the magnitude of the cross-sectional velocity scales are also equal – the viscosity contour levels are exponentially spaced. They show the degree of unsteadiness in the flow as well as the degree to which the major unsteady structures are confined to regions close to the pipe wall for the power law and yield stress fluids, whereas there is a significantly increased degree of structure in the core region of the Newtonian fluid. Clearly seen are the lower viscosities (indicative of higher shear rates) in the wall regions in the viscosity contours.

It is interesting to compare the shear-thinning results here to those for viscoelastic fluids presented in [4,5,7]. In those studies, the conclusion was drawn that polymer additives modify the turbulent structure in the buffer layer ($10 < y^+ < 30$) to increase the streamwise vortex size, lessen the streamwise vortex strength, and consequently supply less energy to the log layer. The reduction in advective transport of high-momentum fluid from the core toward the wall ultimately leads to the prediction of drag reduction. Correlated to the weaker vortices

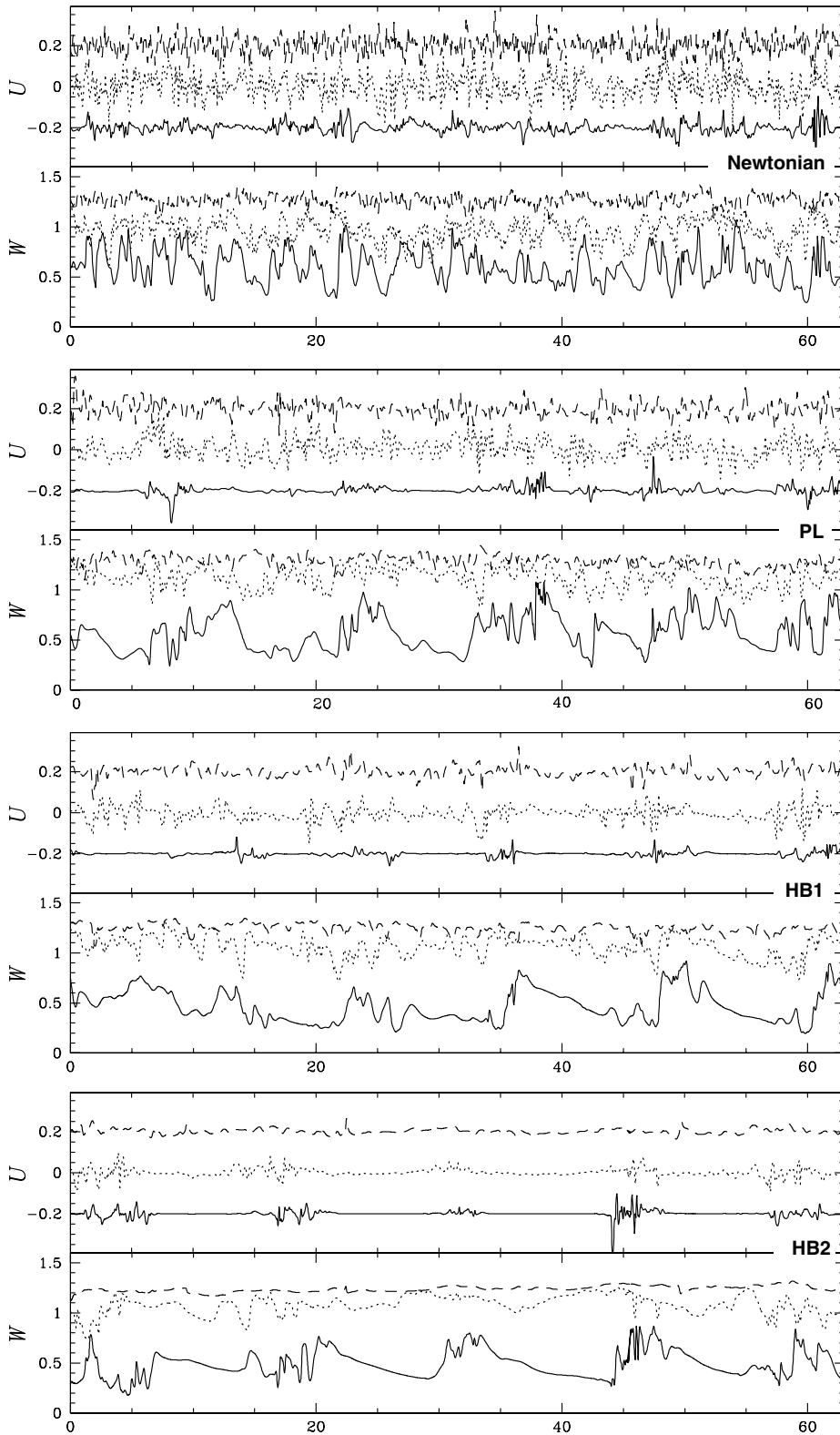


Fig. 9. Wall-normal (U) and axial (W) velocity signals at three radial locations for Newtonian fluid (top), PL, HB1, and HB2 (bottom). The dashed line is at the pipe centreline, the dotted line is in the log layer ($y^+ \approx 85$) and the solid line is near the pipe wall ($y^+ \approx 10$). The elapsed time is approximately 5 domain transit times. Note that for the wall normal profiles, the near wall and centreline traces have been offset by -0.2 and 0.2 respectively to allow the three traces to be distinguished – the mean value for all wall normal velocity traces is zero.



Fig. 10. Predicted axial velocity at $y^+ \approx 20$ for $Re_G = 7500$. From top to bottom, Newtonian, PL ($n = 0.6$, $\tau_Y = 0$), HB1 ($n = 0.6$, $\tau_Y = 0.1\tau_w$), HB2 ($n = 0.6$, $\tau_Y = 0.5\tau_w$). The pipe surface has been rolled flat and the flow is from left to right. White represents high velocity and black low.

were reduced wall normal and spanwise velocity fluctuations compared to the Newtonian case (these correspond to radial and azimuthal fluctuations here). It was also observed that streamwise (axial) fluctuations were slightly higher than the Newtonian case. As the degree of visco-elasticity increased, these trends increased and it was seen that the slope of the mean velocity log layer increased also. The majority of these phenomena are similar in character to those observed here when “degree of viscoelasticity” is replaced by “magnitude of shear stress”. Recall that the simulation results here are for fluids that have no visco-elasticity. The cause of the phenomena here is simply the increased viscosity near the core of the flow (i.e. in lower shear regions) that dampens the turbulent structures and reduces radial momentum transfer.

4.4. Summary of pipe flow results

Adding a yield stress to a power law fluid (i.e. “creating” a Herschel–Bulkley fluid) has a marked difference to the fluid’s turbulent flow in a pipe. Similar to power law fluids, the increased viscosity in the core of the flow results in weaker turbulence structures in the near-wall region that advect less of the high speed core flow toward the wall, hence reducing the non-dimensionalised drag (for a fixed Re_G). In addition, the effect of increasing yield stress (again for a fixed Re_G) is to accentuate these effects, to the point where a yield stress

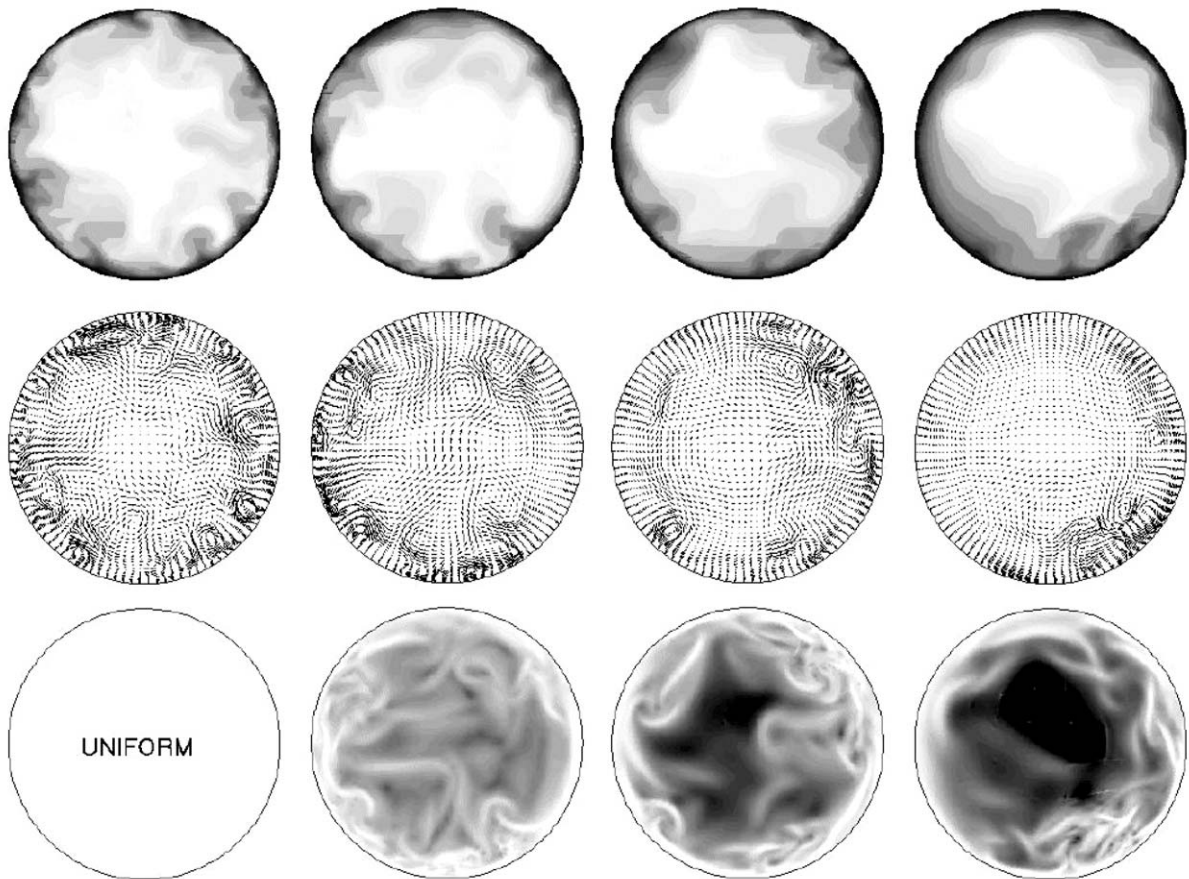


Fig. 11. Instantaneous contours of axial velocity, cross-stream velocity vectors, and viscosity contours for Newtonian, PL, HB1 and HB2 simulations ($Re_G = 7500$). For axial velocity, white contours are high and black low. For viscosity, white is low viscosity and black high.

equal to one half the mean wall shear stress of the power law case renders the flow transitional at $Re_G = 7500$ – a Reynolds number that is well-developed turbulence in the case of a Newtonian fluid. As the yield stress increases, the core of the flow becomes increasingly laminar, and it appears possible that a sufficient yield stress (perhaps combined with a small flow index, n) may allow a completely laminar, even plug, flow in the core to co-exist with unsteady transitional and/or turbulent wall layers. This was not seen in the examples considered here, and attempts to increase the yield stress beyond the maximum value used above led to an unstable simulation that required impractically small time-steps to run successfully. Nevertheless, this possibility is intriguing and may be one way of transporting significant solids in a stable plug at the same time as re-suspending those solids that are able to settle as a result of pipe bends, etc.

5. Blood flow in a channel

In [9] a RANS (Reynolds-Averaged Navier–Stokes) approach with a modified Spallart–Allmaras turbulence model [22] was used to simulate the flow of blood (modelled rheologically as a Carreau–Yasuda fluid) in a channel flow domain. Referring to Eq. (4), the appropriate rheology parameters for blood are $\eta_0 = 1.612 \times 10^{-1} \text{ kg m}^{-1} \text{ s}^{-1}$, $\eta_\infty = 3.527 \times 10^{-3} \text{ kg m}^{-1} \text{ s}^{-1}$, $\lambda = 8.2 \text{ s}$, $a = 1.23$, $b = 0.64$ [9]. Kinematic viscosity is required in the subsequent non-dimensionalisation and is determined by dividing dynamic viscosities by the density of blood, taken to be $\rho = 1058 \text{ kg m}^{-3}$.

To compare to these RANS simulation results, a DNS simulation was undertaken in a rectangular channel with a streamwise length of $5\pi D$ and a spanwise height of $2\pi D$ where D is the channel half width. The wall

normal (x), spanwise (y) and streamwise (z) velocity components are labelled (U , V , W) respectively. The domain was discretised using 70 21×21 elements in the cross-stream plane and 192 z -planes (96 complex Fourier modes) in the streamwise direction. This provided a near-wall mesh resolution of approximately $x^+ \approx 0.2$, $y^+ \approx 6$ and $z^+ \approx 15$. The wall-normal mesh spacing near the channel centre was $x^+ \approx 5$, which is sufficient for good resolution of this flow. Physically, the channel half-width was chosen to be $D = 10$ cm.

The simulation parameters were chosen to provide a friction velocity Reynolds number (Re_τ) of 180. The definition of friction velocity and friction velocity Reynolds number allows the wall shear rate to be written as

$$\dot{\gamma}_w = (Re_\tau/h)^2 v_w, \tag{9}$$

which is substituted into the Carreau–Yasuda model (Eq. (4)) estimated at the wall. The resulting implicit equation for the mean wall viscosity, v_w , is solved iteratively. The mean wall viscosity is then used to calculate the friction velocity (via the definition of Re_τ), the mean wall shear stress and pressure gradient. To estimate a priori the resulting superficial velocity, a Blasius turbulent flow profile with a kinematic viscosity equal to $v_\infty (= \eta_\infty/\rho)$ was assumed, and finally this mean superficial velocity was used in the non-dimensionalisation of the problem. A similar process could have been used with v_w instead of v_∞ , but either approximation leads to an error of approximately 10% in the superficial velocity predicted from the DNS (Table 4).

5.1. Results

The mean streamwise velocity profile for the Carreau–Yasuda fluid is plotted in wall units in Fig. 12 and compared to the RANS results of [9] and Newtonian results at the same value of Re_τ . As seen, the profile lies above that of a Newtonian fluid, suggesting that the flow is either not well developed turbulence, or that the basic profile is significantly different. Despite lying significantly above the Newtonian profile, the slope of the Carreau–Yasuda log-layer region is very similar to the Newtonian fluid, which is in contrast to the power law results presented in [6] and the Herschel–Bulkley results above (for HB2). The Spallart–Allmaras turbulence model provides quite reasonable estimates of the mean flow profile over most of the range, although there is some discrepancy in the buffer layer.

Table 4
Non-dimensional parameters for the channel flow simulation

Model	v_∞	v_0	v_w	K	$\partial P/\partial z$	Actual W	Re_G
Carreau–Yasuda	1.914×10^{-4}	8.749×10^{-3}	3.427×10^{-4}	14.2817	3.805×10^{-3}	1.101	3214

Re_G is based on channel half width, superficial velocity and wall viscosity.

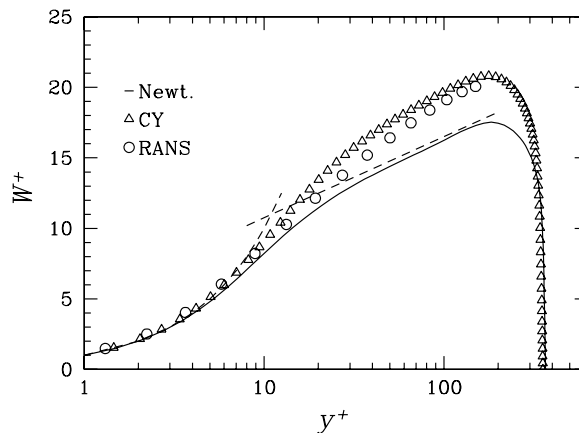


Fig. 12. Mean streamwise velocity profile for DNS of a Carreau–Yasuda fluid (Δ) and RANS results presented in [9] (\circ). The Newtonian profile for the same value of Re_τ is shown as the solid line.

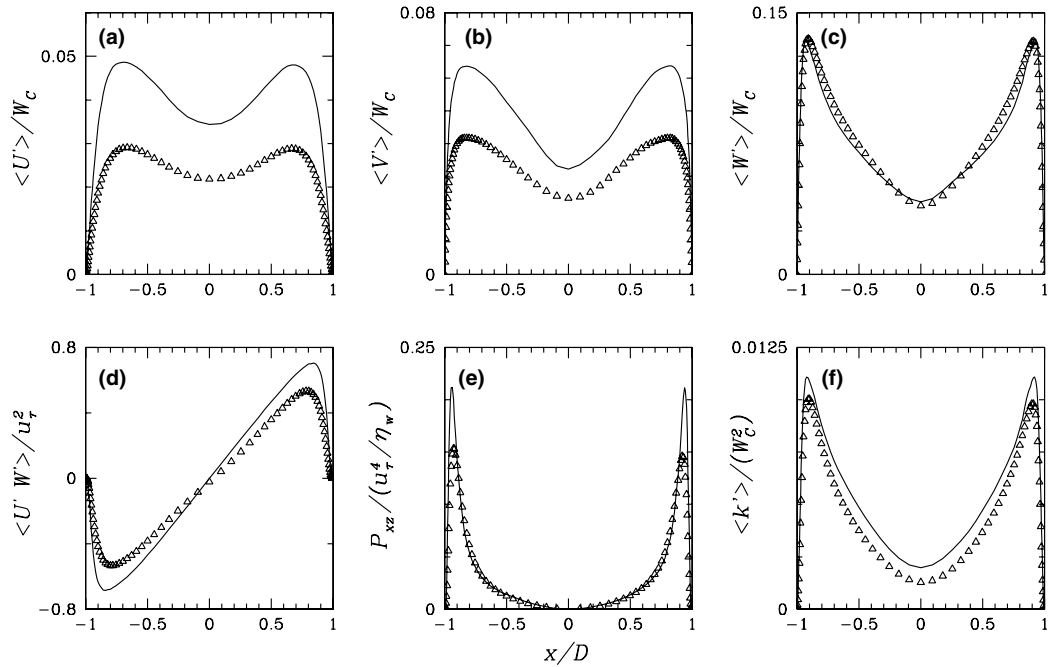


Fig. 13. Second-order turbulence statistics for the channel flow of a Carreau–Yasuda fluid (Δ) and Newtonian fluid (solid line).

The second-order turbulent statistics are shown in Fig. 13, where it is seen that the cross-stream turbulence intensities for a Carreau–Yasuda fluid in a channel are significantly lower than the Newtonian values, but that the streamwise fluctuation is marginally higher across most of the channel width. All in all, the turbulent kinetic energy is slightly lower than the Newtonian value. Reynolds stresses and turbulence production follow similar trends to pipe flow of both power law and Herschel–Bulkley fluids.

The mean viscosity profile (normalised by the mean wall viscosity) is shown in Fig. 14. The mean centreline viscosity is six times that of the wall (although still five times lower than the zero-shear viscosity). As expected, the lower shear rates near the centreline result in increased viscosity there and, as with the pipe flow results above, reduce the cross-stream turbulence intensities (Fig. 13) and reduce momentum transport to the wall.

For this fluid, the non-Newtonian rheology has a significant impact on the near-wall structures in the turbulent boundary layer as seen in the predicted near-wall streaks (at $x^+ \approx 20$) shown in Fig. 15. The streak spacing is significantly larger, and the streak length significantly longer with several streaks spanning the entire

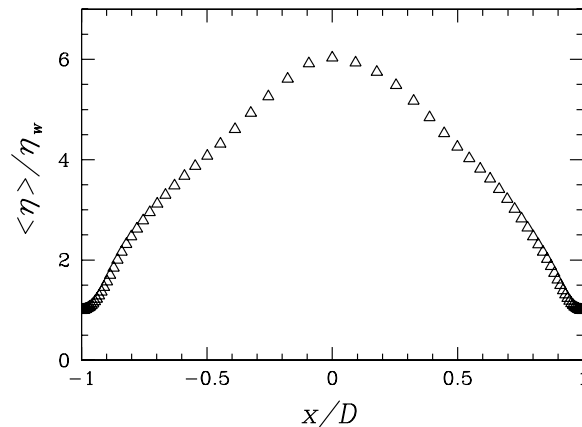


Fig. 14. Mean viscosity profile of a turbulent Carreau–Yasuda fluid (non-dimensionalised by the wall viscosity).

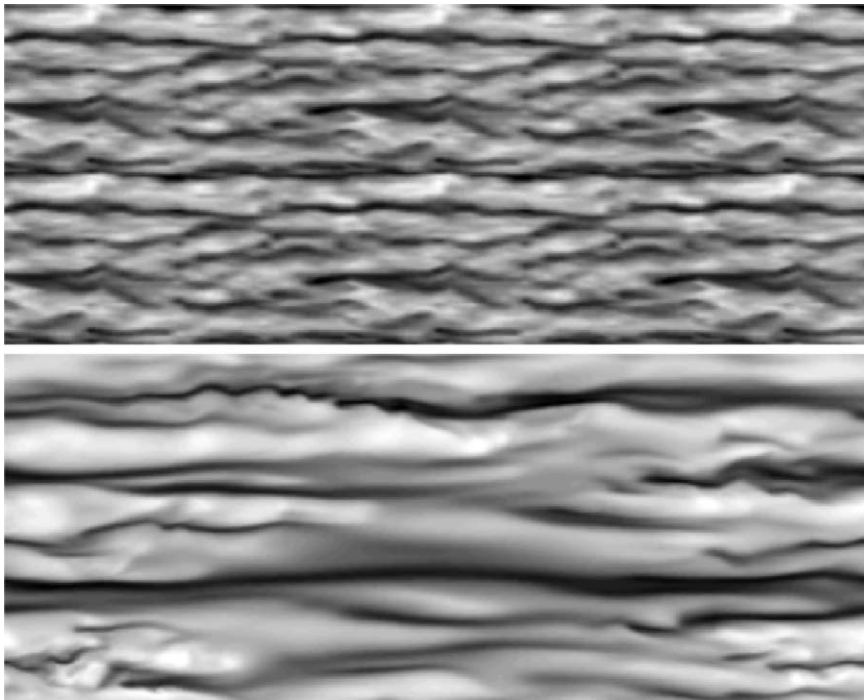


Fig. 15. Wall streaks for Newtonian channel flow (top) and Carreau–Yasuda fluid (bottom) at a distance of $x^+ \approx 20$. Flow is from left to right. (Note that the Newtonian case was calculated on a smaller domain and a number of data repetitions in the streamwise and spanwise directions have been included to show the same area as the Carreau–Yasuda case. The joins between the images are visible, especially in the spanwise direction.)

domain length, suggesting that the streamwise extent of the domain should be increased for reliable simulation of this flow. Fig. 16 shows instantaneous cross-sections of the axial velocity, cross-stream velocity vectors and viscosity. As in the pipe flow simulations, the turbulent structures confined to the regions close to the wall, with relatively little turbulent structure toward the centre of the flow. This is consistent with the turbulence intensities shown in Fig. 13, and is again related to the higher viscosities there. The results for this fluid in a channel flow domain are qualitatively similar to pipe flow of power law and Herschel–Bulkley fluids, and no significant differences emerge from them.

6. Summary of results

A numerical method for the Direct Numerical Simulation of the turbulent flow of generalised Newtonian fluids is outlined, and its parallel implementation using MPI discussed. It is seen that as the number of processors increases, the method becomes less efficient (56% as efficient with 48 CPUs as with 1) however the wall time for turning a simulation around is thirty times less. Comparing an eight hour wait to a ten day wait for a simulation to run suggests that the loss in efficiency is generally an acceptable trade-off.

The results for all the non-Newtonian fluids above are consistent with those found for turbulent pipe flow of power law fluids in [6], with larger, weaker turbulent structures for the non-Newtonian fluids compared to Newtonian and smaller friction factors at a fixed Re_G . The addition of a yield stress to a power law fluid weakens the structures still further, driving the flow more toward the transitional regime. Additionally, the mean flow profile deviates further from the Newtonian and power law profiles as a yield stress increases.

It appears that pipe flow of yield stress fluids make the transition to turbulence via intermittency and turbulent events like the slugs and puffs observed in Newtonian flow (see Fig. 10). Although the results are not conclusive because of the insufficient domain length of the simulations, they are believed to be qualitatively correct. These unsteady structures may potentially be able to resuspend small settling particles in particle-

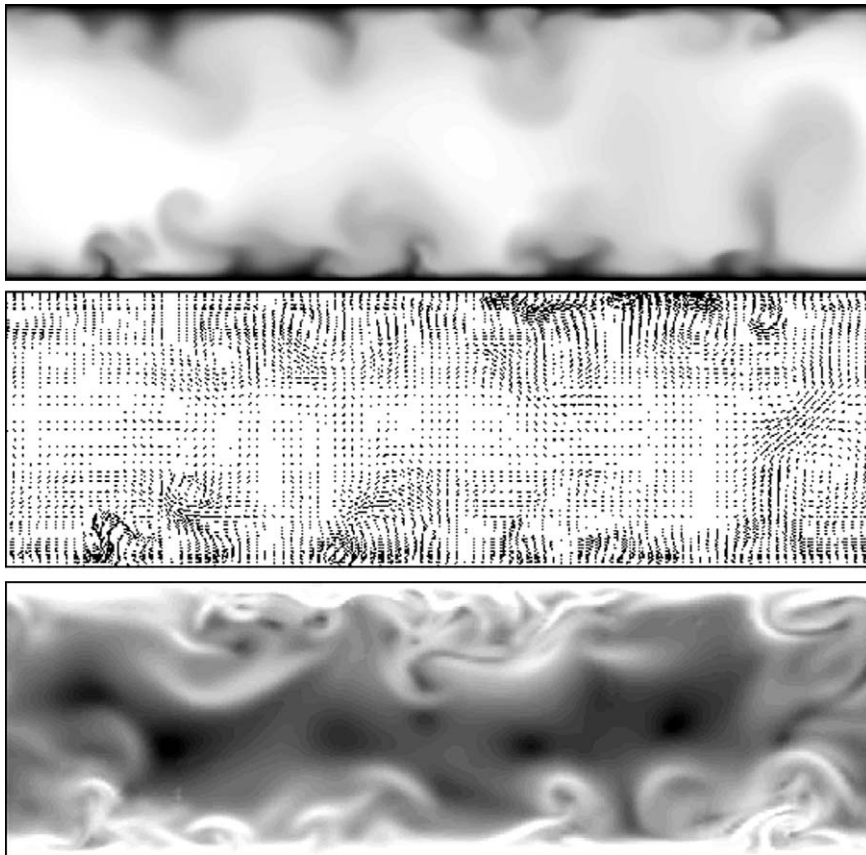


Fig. 16. Instantaneous contours of streamwise velocity (top), velocity vectors (middle) and contours of viscosity (bottom) for the channel flow of a Carreau–Yasuda fluid. Black is slow and white fast in the top image and black is high viscosity and white low in the bottom figure.

laden flows, allowing the transitional regime to be possible for suspension transport in yield stress carrier fluids.

Simulation of a Carreau–Yasuda fluid showed similar behaviour to the Herschel–Bulkley results, with log-law profiles that lay above the Newtonian profile (suggesting undeveloped flow) and velocity fluctuations with similar behaviour. Like the Herschel–Bulkley flow (especially at the higher yield stress), the Carreau–Yasuda flow was transitional, even at a generalised Reynolds number of 3214.

When using polymer solutions to approximate idealised rheologies, difficulties can be encountered in understanding and interpreting experimental results due to the presence of unwanted rheological effects (e.g. viscoelasticity). The application of this DNS technique to flows of non-Newtonian fluids allows the rheology model to be treated with certainty and has the potential to enable the effect of different rheological parameters to be correctly quantified and understood. This is a significant contribution that DNS can bring to the study of flows of non-Newtonian fluids. However, a key problem in obtaining accurate results of turbulent flow of real non-Newtonian fluids using DNS is the difficulty in approximating a real fluid rheology over a very wide range of shear rates using any of the simple generalised Newtonian rheology models. It is likely that this limitation in measurement will ensure that accurately modelling the turbulent flow of real fluids will remain a difficult task.

Acknowledgements

The authors gratefully acknowledge Dhruv Arora, Department of Mechanical Engineering and Material Science at Rice University, Texas, for providing his results for RANS modelling of blood flow.

References

- [1] M.P. Escudier, F. Presti, Pipe flow of a thixotropic liquid, *J. Non-Newton. Fluid Mech.* 62 (1996) 291–306.
- [2] M.P. Escudier, F. Presti, S. Smith, Drag reduction in the turbulent pipe flow of polymers, *J. Non-Newton. Fluid Mech.* 81 (1999) 197–213.
- [3] F.T. Pinho, J.H. Whitelaw, Flow of non-Newtonian fluids in a pipe, *J. Non-Newton. Fluid Mech.* 34 (1990) 129–144.
- [4] N. Beris, C.D. Dimitropoulos, Pseudospectral simulation of turbulent viscoelastic channel flow, *Comput. Methods Appl. Mech. Eng.* 180 (1999) 365–392.
- [5] E. De Angelis, C.M. Casciola, R. Piva, DNS of wall turbulence: dilute polymers and self-sustaining mechanisms, *Comput. Fluids* 31 (2002) 495–507.
- [6] M. Rudman, H.M. Blackburn, L. Pullum, L.J.W. Grahan, Turbulent pipe flow of shear thinning fluids, *J. Non-Newton. Fluid Mech.* 118 (2004) 33–48.
- [7] R. Sureskumar, A.N. Beris, A.H. Handler, Direct numerical simulation of the turbulent channel flow of a polymer solution, *Phys. Fluids* 9 (1997) 743–755.
- [8] M.R. Malin, Turbulent pipe flow of power-law fluids, *Int. Commun. Heat Mass Transfer* 24 (1997) 977–988.
- [9] D. Arora, One-equation turbulence model for generalized Newtonian fluid flow, Rice University Preprint, 2004.
- [10] K.C. Wilson, A.D. Thomas, A new analysis of the turbulent flow of non-Newtonian fluids, *Can. J. Chem. Eng.* 63 (1985) 539–545.
- [11] A.D. Thomas, K.C. Wilson, New analysis of non-Newtonian turbulent flow – yield-power-law fluids, *Can. J. Chem. Eng.* 65 (1987) 335–338.
- [12] R. Stainsby, R.A. Chilton, in: *Pumping Sludge and Slurry*, Ipswich Book Company, 1998, pp. 13–30.
- [13] G.E. Karniadakis, Spectral element—Fourier methods for incompressible turbulent flows, *Comput. Methods Appl. Mech. Eng.* 80 (1990) 367–380.
- [14] G.E. Karniadakis, M. Israeli, S.A. Orszag, High-order splitting methods for the Navier–Stokes equations, *J. Comput. Phys.* 97 (1991) 414–443.
- [15] J.L. Guermond, J. Shen, Velocity-correction projection methods for incompressible flows, *SIAM J. Numer. Anal.* 41 (2003) 112–134.
- [16] G.E. Karniadakis, S.A. Orszag, V. Yakhot, Renormalization Group theory simulation of transitional and turbulent flow over a backward-facing step, in: Galerpin, Orszag (Eds.), *Large Eddy Simulation of Complex Engineering and Geophysical Flows*, CUP, 1993, pp. 159–177.
- [17] H.M. Blackburn, LES of turbulent channel flow using spectral elements, in: *13th A/Asian Fluid Mech. Conf.*, Melbourne, 1998.
- [18] M. Rudman, H.M. Blackburn, Large eddy simulation of turbulent pipe flow, in: *2nd Int. Conf. on CFD in the Minerals and Process Ind.*, Melbourne, 1999.
- [19] S. Schmidt, D.M. McIver, H.M. Blackburn, M. Rudman, G.J. Nathan, Spectral element based simulation of turbulent pipe flow, in: *14th A/Asian Fluid Mech. Conf.*, Adelaide, 2001.
- [20] J.M.J. den Toonder, F.T.M. Nieuwstadt, Reynolds number effects in a turbulent pipe flow for low to moderate Re, *Phys. Fluids* 9 (11) (1997) 3398–3409.
- [21] D.W. Dodge, A.B. Metzner, Turbulent flow of non-Newtonian systems, *AIChEJ* 5 (1959) 189–204.
- [22] P.R. Spallarat, S.R. Allmaras, A one-equation turbulence model for aerodynamic flows, AIAA Paper 92-04399, AIAA 30th Aerospace Sciences Meeting, 1992.